ACS APPLIED ENERGY MATERIALS

www.acsaem.org Article

Boosted Oxygen Evolution Reaction in Bimetallic Alloy Nanoparticles/Carbon Composite via Simple One-Step Molten Salt-Assisted Synthesis

Xueda Liu, Dongyuan Song, Quan Quan, Dong Chen, Hikaru Saito, Liyuan Dai, Midori Ikeuchi, Takeshi Yanagida,* Johnny C. Ho,* and SenPo Yip*

Cite This: *ACS Appl. Energy Mater.* 2025, 8, 3449−3458 Read Online

ACCESS | Metrics & More | Article Recommendations | Supporting Information

ABSTRACT: The growing need for energy conversion technologies has stimulated the development of innovative electrocatalysts designed explicitly for oxygen evolution reactions (OER). Nonprecious metal/carbon-based composites are widely studied for this purpose due to their low cost and unique structures. However, conventional methods for preparing transition metal/carbon composites are often cumbersome and time-consuming. These methods have other disadvantages, such as poor catalyst uniformity, limited potential for surface modification, and excessive oxidation of metal particles. In this work, we employed a simple one-step molten salt (MS) method to synthesize FeNi alloy/carbon composites. The sample prepared by the MS strategy, with an optimal Fe/Ni ratio, performs a low overpotential of 279.4 mV at a current density of 10 mA cm^{-2} and a small Tafel slope of 45.7 mV dec^{-1}. Compared with the sample prepared through traditional pyrolysis, the sample prepared by the MS method demonstrates modulated and optimized surface characteristics for both the carbon support and metallic particles. Furthermore, the synthetic process enables the uniform growth of alloy particles on the carbon substrate. These structural improvements result in abundant defects and active sites, significantly enhancing OER activity. Overall, this work highlights the role of the MS method in promoting the catalytic activity of FeNi alloy/carbon composites. This research contributes to advancing non-noble metal electrocatalysts for future catalytic applications.

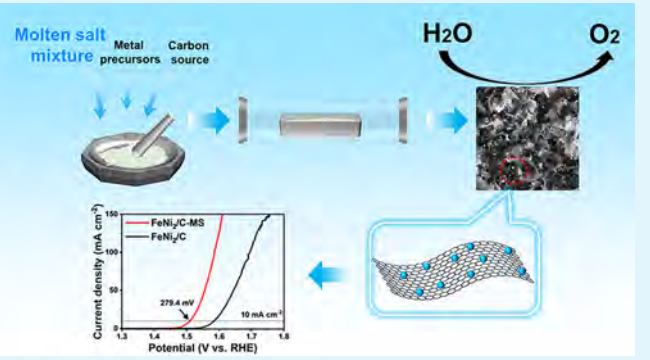

KEYWORDS: *oxygen evolution reactions, molten salt method, one-step synthesis, FeNi alloy/carbon composite, efficient catalytic performance*

1. INTRODUCTION

The pollution produced by the overuse of fossil fuels, such as natural gas, coal, and oil, has become one of the most pressing problems faced by human society.[1−3] Hydrogen holds promise as a clean energy source, offering high energy density and zero carbon emissions upon consumption.[4] Incorporating hydrogen into the energy grid could reduce our reliance on environmentally harmful fossil fuels.[5] However, an efficient way to produce hydrogen still needs to be developed to enable widespread commercialization. Currently, industrial-scale hydrogen is mainly produced by processes like natural gas reforming, which generates significant CO_2 emissions. In contrast, renewable energy-powered water splitting is considered a potential strategy for hydrogen production, enabling the efficient conversion between electrical and hydrogen energy to realize flexible energy utilization.[6]

Electrochemical water splitting is a process that separates water molecules into hydrogen and oxygen gases through two half-reactions: the hydrogen evolution reaction (HER) and the oxygen evolution reaction (OER).[7] It is widely recognized that the OER is significantly more kinetically sluggish and requires a much higher overpotential than the HER. This limitation reduces water-splitting efficiency and impedes the development of a hydrogen production industry based on this process.[8] To enhance the kinetics and efficiency of the OER, the development of high-performance and cost-effective electrocatalysts is critical. Noble metal-based oxides, such as IrO_2 and RuO_2, are currently regarded as benchmark electrocatalysts for the OER. However, their high price hinders their widespread application.[9] Consequently, the design and development of non-noble metal-based electrocatalysts have

Received: November 19, 2024
Revised: February 21, 2025
Accepted: February 24, 2025
Published: March 3, 2025

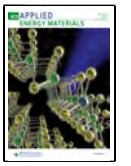

become a priority. In this regard, transition metals—particularly iron (Fe), cobalt (Co), and nickel (Ni)[10]—along with their oxides,[11] hydroxides,[12] sulfides,[13] nitrides,[14] and other derivatives,[15,16] have attracted significant attention. These materials are promising candidates for OER electrocatalysis due to their low cost and high efficiency. Alloys composed of transition metals demonstrate excellent electrocatalytic activity for the OER, attracting considerable interest from many researchers.[17−19] Among these, the FeNi alloy has been extensively studied as an OER electrocatalyst due to its low cost, remarkable catalytic activity, and durability. FeNi alloy also shows significantly higher OER activity than pure Ni or Fe catalysts.[20] Furthermore, integrating FeNi alloys with carbon-based materials, such as graphene[21] and carbon nanotubes,[22] has been shown to further boost OER activity, providing a unique opportunity to enhance the overall efficiency of the water-splitting process.

Conventional synthesis methods for bimetallic FeNi/carbon composites typically involve multiple steps, such as encapsulation, calcination, alloying, and so on, which are tedious, laborious, and time-consuming, limiting their potential for large-scale production.[23,24] Additionally, alloy particles are prone to oxidation during high-temperature synthesis, forming excessive metal oxide layers.[25,26] Another challenge is to achieve a uniform distribution of bimetallic particles on the carbon support. Interactions between different metal atoms can cause uncontrolled migration and segregation. This results in accumulation and uneven particle distribution, ultimately reducing the availability of active sites.[27,28] Therefore, developing a simpler, faster, and more environmentally friendly alternative synthesis method is essential to overcome these issues and facilitate the large-scale practical application of alloy/carbon catalysts.

This study investigates the potential of a one-step molten salt (MS) method for fabricating bimetallic metal particles and carbon composites as highly efficient OER electrocatalysts. The MS method is considered environmentally friendly due to the recyclability of salt after recrystallization and the wide choice of renewable carbon sources, such as biomass, polymers, and small organic molecules.[29,30] Our work pointed out that a key advantage of the MS method lies in its dual functionality, enabling simultaneous modification of the graphite substrate and the surface of the metallic component. This integrated process results in the synthesized composites' unique structural and catalytic properties. The obtained composites exhibit excellent OER performance, achieving an overpotential of 279.4 mV at a current density of 10 mA cm^{-2} and a Tafel slope of 45.7 mV dec^{-1}, placing them among the best-performing transition-metal-based electrocatalysts operating in alkaline electrolytes. The superior catalytic performance can be attributed to several synergistic effects facilitated by the MS method. First, the method optimizes the carbon substrate by enhancing its specific surface area and introducing abundant defect sites that serve as additional reactive centers. Second, the molten salt medium provides ideal conditions for the uniform deposition and distribution of metal particles. Moreover, it modifies the surface of the metallic nanoparticles, further boosting catalytic activity. By integrating these beneficial features, the MS method enables the production of high-performance metal−carbon composites with advanced structural and functional properties. The insights gained from this study offer a foundation for further innovation in catalyst synthesis, highlighting the molten salt method as a versatile and sustainable approach for next-generation electrocatalysts.

2. EXPERIMENTAL SECTION

2.1. Materials. Nickel chloride hexahydrate ($NiCl_2·6H_2O$, 98%), iron chloride tetrahydrate ($FeCl_2·4H_2O$, ≥99%), sodium chloride (NaCl, 99.5%), potassium chloride (KCl, 99.5%), glucose ($C_6H_{12}O_6$), Nafion (5 wt %), ethanol (≥99.5%), and potassium hydroxide (KOH, 85%) were obtained from Fuji Film Co., Ltd. (Osaka, Japan). Ruthenium oxide (RuO_2, 99.9%) was purchased from Sigma-Aldrich Co., Ltd. (St. Louis, USA). The graphite rod was acquired from Narika Co., Ltd. (Tokyo, Japan). The Ag/AgCl electrode (NaCl saturated) and glassy carbon electrode were purchased from ALS Co., Ltd. (Tokyo, Japan). All the chemicals were used directly without further purification.

2.2. Material Synthesis. The synthesis procedures of the $FeNi_2$/C-MS are exhibited in Figure 1a. Typically, 0.02 g of metal precursors

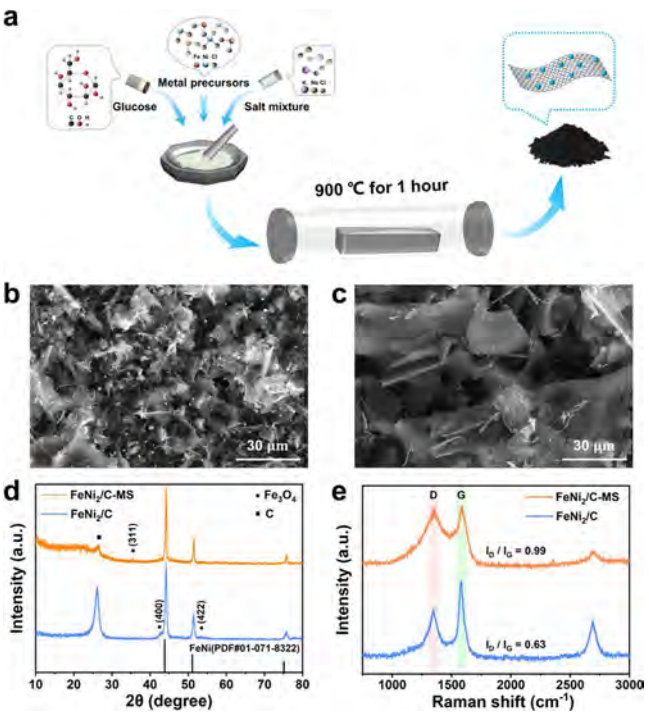

Figure 1. (a) Schematic illustration of the preparation of $FeNi_2$/C-MS. (b) SEM image of $FeNi_2$/C-MS; (c) SEM image of $FeNi_2$/C. (d) XRD patterns of $FeNi_2$/C-MS and $FeNi_2$/C. (e) Raman spectra of $FeNi_2$/C-MS and $FeNi_2$/C.

of $FeCl_2·4H_2O$ and $NiCl_2·6H_2O$ (with the molar ratio of 1:2), 0.1 g of glucose, and 1 g of a salt mixture of NaCl and KCl (with the molar ratio of 1:1) were weighed and ground using a mortar and pestle for 15 min. The well-mixed powder was transferred into an alumina crucible and moved to a tube furnace. After argon was purged in the quartz tube with a flow rate of 250 mL/min for 1 h at 20 °C, the temperature was raised to 900 °C with a heating rate of 10 °C min^{-1} and kept at 900 °C for 1 h. Following this, the heating process was automatically stopped, and argon gas was kept on until the furnace naturally cooled down to room temperature. Finally, as shown in Figure S1, the black powder was obtained by washing the obtained product with sufficient DI water and drying it in a vacuum oven at 50 °C for 2 h, denoted as $FeNi_2$/C-MS. The reference sample $FeNi_2$/C was prepared by direct pyrolysis using the same route without adding the NaCl/KCl mixture.

In addition, by changing the molar ratio of metal precursors ($FeCl_2·4H_2O$ and $NiCl_2·6H_2O$) to 1:1 and 2:1, final samples loaded with FeNi nanoparticles in different FeNi ratios were obtained and

https://doi.org/10.1021/acsaem.4c02958
ACS Appl. Energy Mater. 2025, 8, 3449−3458

named FeNi/C-MS and Fe_2Ni/C-MS, respectively. Meanwhile, the reference samples of FeNi/C-MS and Fe_2Ni/C-MS were prepared using the same procedure, except for adding the eutectic salt, and they were named FeNi/C and Fe_2Ni/C, respectively.

2.3. Electrochemical Measurements. All electrochemical measurements were tested in a three-electrode system by using an electrochemical workstation (Gamry 1010E, USA). The three electrodes in this study involved a graphite rod serving as the counter electrode, a saturated Ag/AgCl as the reference electrode, and a glassy carbon electrode, with a 3.0 mm diameter. The preparation of the working electrodes included several steps. Initially, 5 mg of sample powder was dispersed in 340 μL of ethanol and 20 μL of Nafion (5 wt %). Following a 90 min sonication to form a homogeneous solution, 2 μL of the resulting ink was dropped on the surface of the glassy carbon electrode polished with aluminum oxide powder. The preparation of the RuO_2 working electrode used as the benchmark for OER was the same as the preparation of the sample working electrode above, except that the sample powder was replaced with 5 mg of RuO_2 powder. The loading density of the catalysts was around 0.393 mg cm^{-2} for all of the tested samples. A 1 M KOH solution was employed for electrochemical measurements of the catalysts after purging the electrolyte with O_2 for 15 min. All measured potentials were converted to the reversible hydrogen electrode (RHE) with the following equation: $E(\mathrm{RHE}) = E(\mathrm{Ag/AgCl}) + 0.059\ \mathrm{pH} + 0.197$ V. Liner sweep voltammetry (LSV) was utilized to obtain the polarization curves at a scanning rate of 10 mV s^{-1}, and the data were corrected by IR compensation. The Tafel slope was determined according to the Tafel equation of $\eta = b \times \log(j)$, where η indicates the overpotential, j is the current density, and b corresponds to the value of the Tafel slope. Therefore, b was obtained from the corresponding LSV data by fitting η versus $\log(j)$. Electrochemical impedance spectroscopy (EIS) was measured at a voltage of 1.51 V vs RHE, using a 5 mV amplitude in the frequency range from 10^5 to 0.01 Hz. The electrochemical active surface area (ECSA) was determined by assessing the non-Faradaic C_{dl} (double-layer capacitance). The C_{dl} was measured by CV at different scan rates from 20 mV to 100 mV s^{-1}. Typically, the C_{dl} is calculated by the formula $C_{dl} = i_c/v$, where i_c represents the double-layer charging current, and v denotes the scanning rate. The ECSA can then be analyzed using the formula ECSA = C_{dl}/C_s, C_s being a standard capacitance value of 0.040 mF/cm^2 in 1 M KOH, as reported by McCrory et al.[31] The durability test was achieved by chronopotentiometry at a current density of 10 mA cm^{-2}.

2.4. Characterization. X-ray diffraction (XRD) scanning was carried out on an X-ray diffractometer (RINT-TTRIII, Rigaku) with Cu Kα radiation (λ = 1.5418 Å). Brunner−Emmett−Teller (BET) surface area analysis and pore size were tested using the BELSORP-mini II. Scanning electron microscopy (SEM) images of the samples and energy-dispersive spectrometry (EDS) were performed on an electron microscope (Helios Hydra CX, Thermo Fisher Scientific) operated at an accelerating voltage of 20 kV. Scanning transmission electron microscopy (STEM) and energy-dispersive X-ray spectroscopy (EDS) were conducted on a Titan Cubed G2 Thermo Fisher Scientific microscope equipped with a four-quadrant windowless super-X silicon drift detector. This microscope was operated at an acceleration voltage of 300 kV. Raman spectra were performed on a Raman spectrometer (Nanofinder30) with 532 nm laser excitation. X-ray photoelectron spectroscopy (XPS) was tested on a Shimadzu/KRATOS Corporation AXIS-165 equipment.

3. RESULTS AND DISCUSSION

The FeNi particles/carbon composite was fabricated by the MS method, denoted as Fe_xNi_y/C-MS, using $FeCl_2{\cdot}4H_2O$, $NiCl_2{\cdot}6H_2O$, and glucose as raw materials and NaCl and KCl serving as solvents when in molten state, as illustrated in Figure 1a. The chemicals were mixed using a mortar and pestle, without using any additional solvent like water or alcohol.[32,33] The molar ratio of NaCl and KCl was chosen to be 1:1, corresponding to the lowest melting point in this system (657 °C).[34] To determine the optimal reaction conditions, samples with a Fe/Ni ratio of 1:2 were prepared at 700, 800, 900, and 1000 °C. These temperatures were chosen to ensure that the salts remained in their molten state. As shown in Figure S2, the sample prepared at 900 °C showed better electrochemical performance than the others. SEM analysis reveals that at synthesis temperatures of 700 and 800 °C, the graphite pieces have larger, smoother surfaces, resulting in lower specific surface areas and reduced catalytic activity (Figure S3). At synthesis temperatures above 900 °C, the graphite pieces become thinner and more porous, increasing the surface area. From the XRD pattern, it can be seen that at 1000 °C, the crystallinity of the graphite is significantly disrupted, suggesting the formation of excessive defects during pyrolysis, collapse of the structure, and a more pronounced degree of oxidation in the metallic components (Figure S4). The decline in catalytic performance at 1000 °C can be attributed to these factors. Therefore, 900 °C was selected as the reaction temperature. At high temperatures, the glucose molecules undergo pyrolysis and are converted into carbon. Additionally, the carbon species during the pyrolysis of glucose may aid in reducing Fe and Ni ion precursors to their metallic form, resulting in the formation of FeNi particles. To optimize the glucose-to-metal chloride ratio for the preparation of Fe_xNi_y/C-MS, samples with varying glucose-to-metal precursor ratios were prepared, and their OER performance was compared. As shown in Figure S5 and Table S5, the optimal ratio of glucose and metal chloride is 5:1 (glucose 0.1 g, metal chloride 0.02 g). The glucose-to-metal precursor ratio and calcination temperature were maintained throughout the study. The Fe_xNi_y/C-MS composites were synthesized with varying Fe and Ni ratios (x and y are x = 1, y = 2; x = 1, y = 1; x = 2, y = 1, respectively). The sample names depend on the molar ratio of the metal precursors ($FeCl_2{\cdot}4H_2O$/$NiCl_2{\cdot}6H_2O$). For comparison, non-MS synthesized counterparts, denoted as Fe_xNi_y/C, were fabricated using the same procedures without addition of NaCl and KCl. According to the existing literature, when the ratio of Fe/Ni reaches 0.5, the catalysts show the highest catalytic activity.[35] Then, we chose the Fe/Ni ratios of 1:1 (metal equimolar sample) and 2:1 (Fe-rich sample) as the control group. The Fe/Ni ratios of the prepared samples ($FeNi_2$/C-MS and $FeNi_2$/C; FeNi/C-MS and FeNi/C; and Fe_2Ni/C-MS and Fe_2Ni/C) were confirmed by SEM-EDS analysis (Figures S6−S8). The EDS spectra of all samples display distinct peaks corresponding to the elements C, O, Fe, and Ni. The data from the accompanying spectra table and Table S2 indicate that the atomic ratio of Fe to Ni closely matches the metal precursor ratios: 1:2 for $FeNi_2$/C-MS, 1:1.9 for $FeNi_2$/C, 1:1.1 for both FeNi/C-MS and FeNi/C, and 1.8:1 and 1.7:1 for Fe_2Ni/C-MS and Fe_2Ni/C, respectively.

The morphologies of the obtained $FeNi_2$/C-MS and $FeNi_2$/C samples were observed by SEM. As shown in Figure 1b,c, the morphology of the catalyst prepared by the MS method differs from that of the catalyst prepared by direct pyrolysis. $FeNi_2$/C-MS exhibits a rough surface with small, thin, layered carbon fragments with some particles evenly attached to the carbon sheets. In contrast, $FeNi_2$/C shows a large, relatively thick carbon support with unevenly distributed small particles. SEM-EDS mappings (Figures S9 and S10) were used further to confirm the composition and properties of the particles. The EDS mappings show that the particles attached to the carbon support are primarily composed of Fe and Ni elements, confirming the presence of FeNi alloy particles. The

https://doi.org/10.1021/acsaem.4c02958
ACS Appl. Energy Mater. 2025, 8, 3449−3458

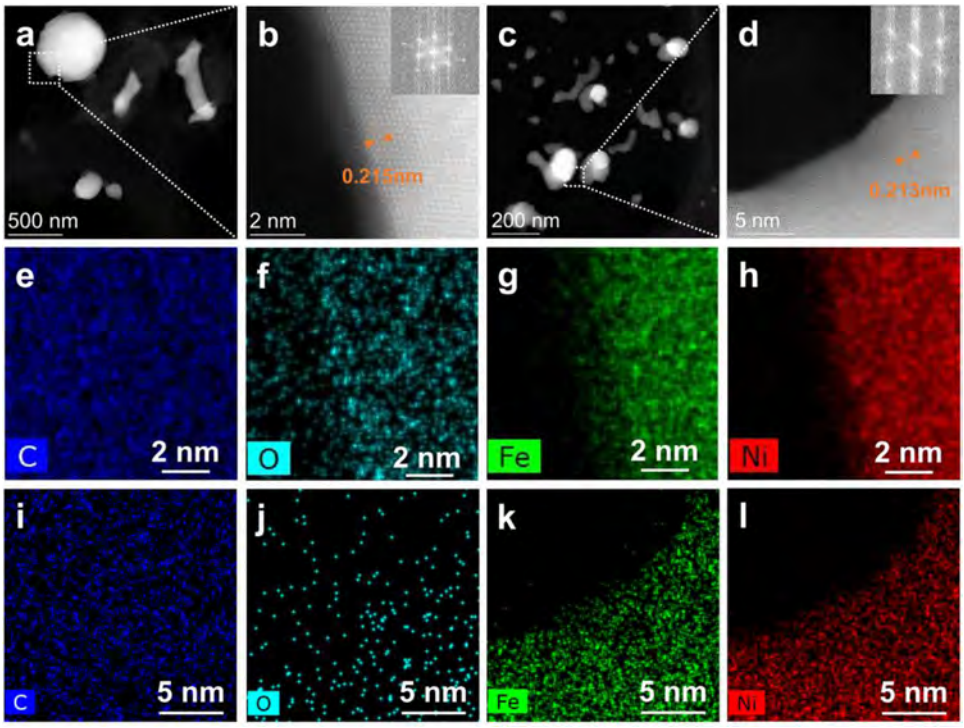

Figure 2. (a) Annular dark-filed (ADF)-STEM image of $FeNi_2$/C-MS; (b) magnified image of a part of (a); (c) ADF-STEM image of $FeNi_2$/C; (d) magnified image of a part of (c); (e–h) EDS elemental maps of $FeNi_2$/C-MS corresponding to (b); and (i–l) EDS elemental maps of $FeNi_2$/C corresponding to (d).

corresponding EDS mappings of Fe and Ni illustrate that the distribution of the metallic FeNi particles differs from the MS-derived and non-MS-derived samples. In $FeNi_2$/C-MS, the FeNi particles are uniformly distributed throughout the samples. At the same time, those for $FeNi_2$/C show an obviously uneven distribution, with the particles frequently concentrating on specific carbon sheets and others showing no particles. This difference in the metal particle distribution can be attributed to the effect of molten salt in $FeNi_2$/C-MS, which facilitates better dispersion of the particles during the synthesis process. When molten salt melts, it creates a stable, homogeneous liquid environment that promotes even metal ion transfer and diffusion. This ensures uniform distribution of metal species during deposition. Its high ionic mobility efficiently transports metal ions to the carbon substrate, leading to a more uniform distribution. By adjusting the temperature and composition of the molten salt, metal deposition can be optimized to prevent agglomeration and ensure uniform particle distribution.[36,37]

In order to investigate whether the morphological differences are affected by the Fe/Ni ratio, plain glucose-derived graphite was fabricated by annealing glucose with and without the addition of molten salt under the same preparation conditions as those for Fe_xNi_y/C-MS but without adding metal precursors. As shown in Figure S11, the plain graphite sample fabricated with MS also exhibits a smaller size than those prepared by direct calcination. Furthermore, the FeNi/C-MS and FeNi/C, as well as Fe_2Ni/C-MS and Fe_2Ni/C, show similar features (Figures S12 and S13). By comparing the SEM images of the three samples fabricated by the MS method with different Fe/Ni ratios—$FeNi_2$/C-MS, FeNi/C-MS, and Fe_2Ni/C-MS—it can be seen that the morphologies of the carbon supports in all three samples are consistent and are not affected by the ratio of metallic components. Therefore, it is concluded that the morphology difference is solely attributed to the MS treatment of glucose. Above its melting point, molten salt acts as a sealing agent, trapping gases such as CO, CO_2, and H_2O released during pyrolysis. The interaction between these trapped gases and carbon promotes the formation of more porous graphite and, hence, the morphological difference.[36] As a result, smaller and thinner carbon fragments are produced. These morphological differences may facilitate rapid electron transport and increase the specific surface area, which is beneficial for electrochemical catalysis.[38] Furthermore, the specific surface area of $FeNi_2$/C-MS and $FeNi_2$/C was investigated by BET. As shown in Table S3, the specific surface area of the samples increases from 227.03 to 266.73 m^2/g when using the MS method, which may be attributed to the structure-directing nature of molten salt.[39] From Figure S14a,b, it can be seen that $FeNi_2$/C-MS shows a type-H4 hysteresis loop, which suggests the existence of narrow slit-like pores.[40] The BJH pore-size distribution curve shows that the pore sizes of $FeNi_2$/C-MS are mainly located at about 1.3, 2.0, and 2.2 nm, indicating the presence of abundant micropores and mesopores. This hierarchical porous structure enhances ion adsorption and accelerates ion transport.[41,42]

The structural information on $FeNi_2$/C-MS and $FeNi_2$/C was obtained by XRD measurements, and the results are shown in Figure 1d. As seen in the XRD patterns, the peak at 26.53° can be attributed to the (002) plane of graphite[43] for both $FeNi_2$/C-MS and $FeNi_2$/C samples. Also, there is a broad diffraction peak between 15° and 30° for $FeNi_2$/C-MS, which suggests that the graphite prepared without the MS method has better crystallinity than that with the MS method. Molten salt is a well-known cause of graphite degradation. When graphite comes into contact with molten salt, various physical

https://doi.org/10.1021/acsaem.4c02958
ACS Appl. Energy Mater. 2025, 8, 3449–3458

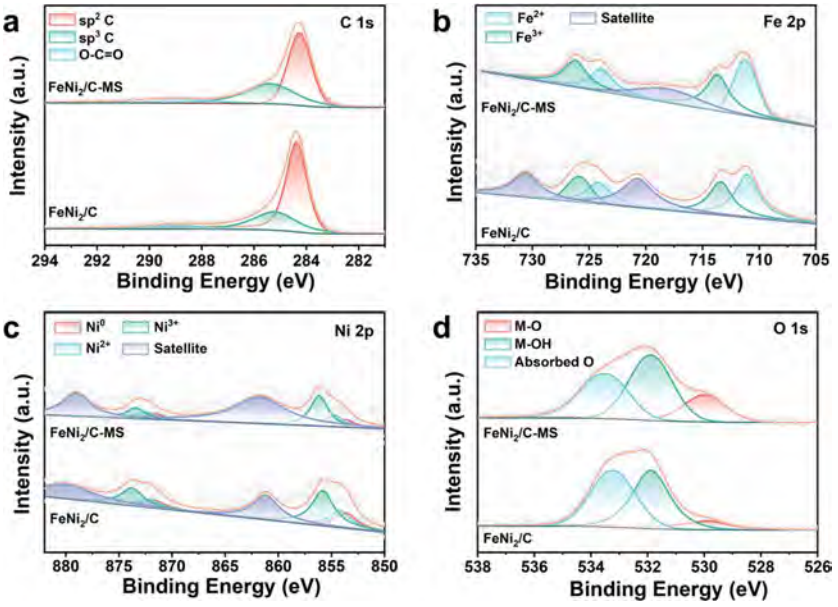

Figure 3. High-resolution XPS spectra of $FeNi_2$/C-MS and $FeNi_2$/C: (a) C 1s (b) Fe 2p; (c) Ni 2p; and (d) O 1s.

and chemical processes—such as infiltration, intercalation, corrosion, and oxidation—can occur, forming new pores, exfoliation, and reduced crystallinity. These effects significantly compromise the integrity of the graphite.[44] On the other hand, three major diffraction peaks around 44.22°, 51.56°, and 75.78° are also observed, corresponding to the face-centered cubic phase of FeNi alloy nanoparticles (PDF#01-071-832), and can be assigned to the (111), (200), and (220) crystal planes, respectively.[45] This indicates that the product primarily comprises the iron−nickel alloy with good crystallinity. Aside from the FeNi alloy and the graphite peaks, weak diffraction peaks originating from iron oxide are observed. A small diffraction peak at 35.60° in the spectrum of $FeNi_2$/C-MS is attributed to the (311) planes of Fe_3O_4 (PDF#01-077-1545). On the other hand, the spectrum of $FeNi_2$/C shows two diffraction peaks at 42.71° and 53.52°, corresponding to the (400) and (422) planes of Fe_3O_4 (PDF#01-077-1545), respectively.[46] These oxide peaks suggest that the metallic particles were slightly oxidized. Samples with different Fe/Ni ratios were also measured by XRD, and the respective spectra show a similar pattern (Figure S15), with diffraction peaks attributed to graphite, FeNi alloy, and Fe_3O_4. However, a significant peak shift (about 0.17°) is observed from the samples of FeNi/C-MS and Fe_2Ni/C-MS, which were prepared with different Fe/Ni ratios of the precursors. This shift suggests that manipulating the precursor ratio can control the metallic particle composition.

Raman spectroscopy was employed to assess the graphitization and degree of defects of the graphite substrate. By analyzing the surface state of carbon in the catalyst by Raman spectroscopy (Figure 1e), two characteristic peaks at 1351.8 cm^{-1} (D-band) and 1582.9 cm^{-1} (G-band) are observed, corresponding to the sp^3-hybridized disordered structures and sp^2-hybridized graphitic carbon, respectively. Furthermore, the I_D/I_G values of the samples are estimated to be 0.99 for $FeNi_2$/C-MS and 0.62 for $FeNi_2$/C. The higher I_D peak ratio of $FeNi_2$/C-MS suggests the possible existence of defects and nanocrystalline phases that can provide active sites for catalytic reactions. At the same time, the I_D/I_G value of 0.99 suggests a moderate degree of graphitization, which is beneficial for transferring charges and electrons.[47] In addition, both $FeNi_2$/C-MS and $FeNi_2$/C exhibit a peak at around 2700 cm^{-1} corresponding to the 2D band, which indicates the stacking status between the graphene layers.

The features of the FeNi metallic particles on the $FeNi_2$/C-MS and $FeNi_2$/C samples were observed using STEM. From Figures 2a,c and S16a,b, metal particles with nonregular shapes are observed. The average particle sizes of the $FeNi_2$/C-MS and $FeNi_2$/C metal particles on the carbon support were determined to be approximately 163 and 66 nm, with standard deviations of 72 and 18 nm, respectively. The significant size difference may be due to the fast transfer of Fe and Ni ions in the molten salt, which accelerates the growth rate of the particles. The magnified images of the selected FeNi particles from both samples are shown in Figure 2b,d, where clear lattice fringes are observed, highlighting the good crystallinity of the metallic particles, which is further confirmed by the clear fast Fourier transform (FFT) images. The interplanar spacing of the adjacent (111) plane is 0.215 and 0.213 nm, respectively, which correspond well with the FeNi alloy.[48] The STEM-EDX mapping shown in Figure 2e−l reveals the C, O, Fe, and Ni distribution in both samples. The distributions of C atoms originating from the graphite substrate are uniform throughout the scanning area. At the same time, an oxygen signal was observed in the metallic particles, with a minor signal appearing on the carbon surface. A stronger oxygen signal is observed in the $FeNi_2$/C-MS sample, which aligns with the XPS observation (discussed later). Lastly, Fe and Ni are distributed uniformly across the metallic particles, suggesting chemical homogeneity.

The surface chemical state of the composite was studied using XPS. Figure S17 shows the overall XPS spectra of $FeNi_2$/C-MS and $FeNi_2$/C, in which the characteristic peaks of the primary elements were highlighted. The XPS spectrum of the prepared sample was analyzed, and it was confirmed that C, Fe, Ni, and O elements exist on the sample's surface, consistent with the results of the EDS mapping. In addition, the atomic ratio of each element is shown in Table S4. Both samples contain around 90 at. % of carbon, which comes from the carbon substrate. However, the atomic ratio of oxygen in

https://doi.org/10.1021/acsaem.4c02958
ACS Appl. Energy Mater. 2025, 8, 3449−3458

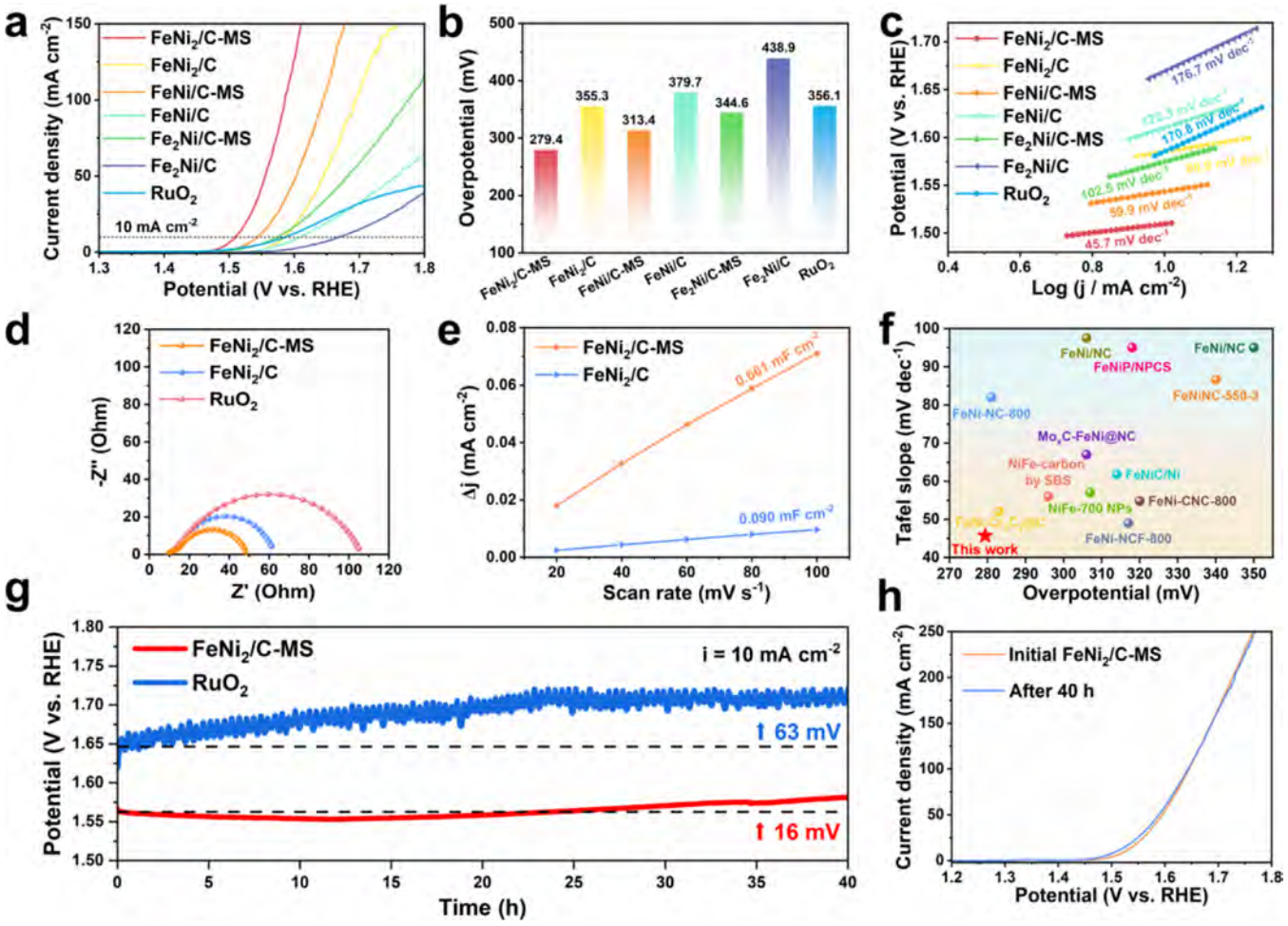

Figure 4. Electrochemical performance of the as-prepared samples and RuO_2. (a) LSV curves; (b) overpotentials at 10 mA cm^{-2} of related catalysts; (c) Tafel slope; (d) electrochemical impedance spectra; (e) plots of the current density of $FeNi_2$/C-MS and $FeNi_2$/C; (f) comparison of the electrocatalytic performance of $FeNi_2$/C-MS with some latest reported non-noble metal-based catalysts; (g) stability test; and (h) LSV curves of $FeNi_2$/C-MS before and after stability tests.

$FeNi_2$/C-MS (9.52%) is 1.4 times that of $FeNi_2$/C (6.76%), in which oxygen probably comes from the breakdown of glucose and the introduction via metal oxidation, carbon−oxygen double bond formation. Figure 3a−d shows the XPS spectrum of $FeNi_2$/C-MS and $FeNi_2$/C of C 1s, Fe 2p, Ni 2p, and O 1s. As shown in the spectrum of C 1s (Figure 3a), the carbon displays three distinct peaks located at binding energies of 284.3, 285.4, and 289.0 eV, corresponding to the sp^2 C (graphitic carbon), sp^3 C (amorphous carbon), and O−C=O (oxidized carbon), respectively.[49] The O−C=O peaks are weaker than the other two peaks, suggesting the lower functionalization degree of carbon.[50] The deconvolution of Fe 2p in Figure 3b shows four contributing peaks of $FeNi_2$/C-MS, the first doublet at 711.2 and 713.7 eV corresponding to Fe $2p_{3/2}$, and the second doublet at 724.3 and 726.2 eV. It can be found that the Fe $2p_{3/2}$ and Fe $2p_{1/2}$ of $FeNi_2$/C are located at 711.0, 713.4, and 724.1, 725.9 eV.[51]This indicates that the MS helps the upshift of the Fe 2p spectra. Figure 3c displays three chemical states 0, 2+, and 3+ of Ni 2p. The peaks at 853.7 and 871.7 eV can be assigned to $2p_{3/2}$ and $2p_{1/2}$ of Ni^0 in $FeNi_2$/C, respectively. The second spectra at 854.2 and 872.2 eV are attributed to $2p_{3/2}$ and $2p_{1/2}$ of Ni^{2+}, respectively. The third peak at 855.8 and 873.6 eV corresponded to $2p_{3/2}$ and $2p_{1/2}$ of Ni^{3+}, respectively. However, by fabricating the sample using MS, the Ni^{2+} and Ni^{3+} peaks in the $2p_{3/2}$ and $2p_{1/2}$ regions are shifted to a higher position (854.7, 872.5, and 856.1, 873.9 eV).[52] These results suggest that charge redistribution occurs during the MS method synthesis. Moreover, the ratios of the high valence states between Fe and Ni increase in $FeNi_2$/C-MS, as shown in Table S5. This indicates that fast electron transfer occurs in the $FeNi_2$/C-MS. The deconvoluted core energy level spectra of O 1s are illustrated in Figure 3d. The observed peaks at 529.6, 531.4, and 533.2 eV correspond to the metal−oxide bond (M−O), hydroxide or oxyhydroxide group (M-OH/OOH), and adsorbed water (H_2O), respectively.[53] From Table S6, it can be seen that $FeNi_2$/C-MS exhibits a higher peak area ratio of M−O (20.7%) and M-OH/OOH (44.1%) than $FeNi_2$/C (13.8%; 41.8%). This indicates that applying the MS method effectively increases the concentrations of M−O and M-OH in $FeNi_2$/C-MS.

The electrocatalytic OER performance of the Fe_xNi_y/C (-MS) and RuO_2 samples was investigated in a standard three-electrode system under 1.0 M oxygen-saturated KOH solution (pH = 14.0). Figure 4a−e shows the electrochemical test results. The polarization curves of the prepared samples and the reference RuO_2 catalyst are displayed in Figure 4a. $FeNi_2$/C-MS exhibits the best OER performance among the six

https://doi.org/10.1021/acsaem.4c02958
ACS Appl. Energy Mater. 2025, 8, 3449−3458

referenced samples, achieving an overpotential of 279.4 mV at a current density of 10 mA cm^{-2}, even lower than that of the RuO_2 catalyst. Compared to other Fe/Ni ratios, the sample with a Fe/Ni ratio of 1:2 exhibits the best electrochemical performance. When Fe is incorporated into Ni, it can not only change the electronic environment of Ni and promote the formation of high-valent Ni, which are active sites for OER, but also enhance the conductivity of the catalyst via partial charge transfer between Fe and Ni.[54,55] However, there is an optimal range for the Fe/Ni ratio that maximizes catalytic efficiency. Excessive Fe incorporation disrupts the Ni active sites and hinders OER activity, while insufficient Fe fails to achieve the desired electronic and structural modifications. Many studies show that the FeNi-based catalysts with 60−90 wt % Ni exhibit optimal electrochemical activity.[56] Sakita et al. also confirmed that catalysts exhibit the highest catalytic activity with an increased charge transfer rate and low charge transfer resistance when the ratio of Fe/Ni reaches 0.5.[35] In addition, when compared with the performance of samples not synthesized by the MS method ($FeNi_2$/C: 355.3 mV, FeNi/C: 379.7 mV, and Fe_2Ni/C: 438.9 mV), as indicated in Figure 4b, the MS-fabricated sample always exhibits a lower overpotential ($FeNi_2$/C-MS: 279.4 mV, FeNi/C-MS: 313.4 mV, and Fe_2Ni/C-MS: 344.6 mV) for all three sets of Fe-to-Ni precursor ratios. This clearly indicates that the MS treatment plays a crucial role in improving electrocatalytic performance. We also evaluated the OER activity of the bare carbon support prepared by MS. From Figure S18, it can be seen that the bare carbon exhibits significantly lower OER activity compared to $FeNi_2$/C-MS, highlighting the contribution of the FeNi as a reaction-active material in the OER. In addition, Tafel plots obtained from the LSV curves (Figure 4c) were employed to analyze the catalytic kinetics of the samples. The Tafel slope value of $FeNi_2$/C-MS (45.7 mV dec^{-1}) is much lower than those of $FeNi_2$/C (60.9 mV dec^{-1}), FeNi/C-MS (59.9 mV dec^{-1}), FeNi/C (120.3 mV dec^{-1}), Fe_2Ni/C-MS (102.5 mV dec^{-1}), Fe_2Ni/C (176.7 mV dec^{-1}), and RuO_2 (170.8 mV dec^{-1}), which reveals its favorable reaction kinetics due to the effect of MS-synthesis samples and optimized Fe and Ni ratio. The electrode kinetics of the prepared catalysts during the OER were analyzed using EIS measurements at 1.51 V versus RHE, as illustrated in Figure 4d. From Figure 4d, samples with the best OER performances, fabricated using both MS and non-MS (i.e., Fe-to-Ni ratio is 1:2), were selected for comparison. The EIS spectra indicate that the charge transfer resistance (R_{ct}) of the catalysts follows this trend: $FeNi_2$/C-MS (R_{ct}, 39 Ω) < $FeNi_2$/C (R_{ct}, 55 Ω) < RuO_2 (R_{ct}, 97 Ω). The smaller R_{ct} value of $FeNi_2$/C-MS compared to those of others suggests a more efficient electron transfer process during the OER. The ECSA was then estimated to compare the catalytic performance of these two samples. The ECSA value is estimated by performing a series of cyclic voltammetry measurements under different scanning rates (20, 40, 60, 80, and 100 mV/s) to evaluate the double-layer capacitance (C_{dl}) (Figure S19). The results were then calculated and summarized in Figure 4e, indicating a linear correlation between the current density and scan rate for both samples. The $FeNi_2$/C-MS sample exhibits a significantly steeper slope of 0.661 mF cm^{-2} compared to the $FeNi_2$/C sample (0.090 mF cm^{-2}), which means the $FeNi_2$/C-MS sample has more active sites and superior OER performances. The intrinsic activity of the samples was evaluated by normalizing the current density using ECSA. The normalizing LSV is shown in Figure S20. These results suggest that $FeNi_2$/C-MS exhibits higher intrinsic catalytic activity during OER. We further compared the performance of $FeNi_2$/C-MS to other non-noble metal-based electrocatalysts in the literature, as summarized in Figure 4f and Table S7. It clearly shows that $FeNi_2$/C-MS exhibits the smallest overpotential and Tafel slope value among those transition-metal-based catalysts operating in alkaline electrolytes. For instance, compared to FeNi-Cr_3C_2/C with an overpotential (η10) of 283 mV,[57] Mo_xC-FeNi/NC with an overpotential (η10) of 306 mV,[58] and FeNiC/Ni with an overpotential (η10) of 314 mV,[59] $FeNi_2$/C-MS stands out with its superior electrochemical activity. The durability of the sample was further examined by performing chronopotentiometry (CP) measurements at 10 mA cm^{-2} in a 1.0 M KOH electrolyte (Figure 4g). $FeNi_2$/C-MS exhibits negligible overpotential loss over 40 h, while RuO_2 shows a significantly larger degradation. The OER performance of the samples before and after the stability test does not decrease significantly (Figure 4h). The fluctuation of the curve is possibly caused by the accumulation and release of bubbles. By directly comparing the SEM images of the catalyst on the glassy carbon electrode before and after the chronopotentiometry test (Figure S21), it can be seen that there is no obvious change in the morphology of the catalyst. The post-test catalyst retains the layered structure, and metal particles could still be observed on the carbon surface. All of these indicate that the sample synthesized by the MS method has strong adhesion between the metal particles and the carbon substrate, thereby giving the composite good structural stability. Overall, by electrochemical evaluation, the samples prepared using the MS method have lower overpotential, better reaction kinetics, faster electron transfer rate, and better OER performance.

4. CONCLUSIONS

In this study, we successfully prepared the Fe_xNi_y/C-MS composite synthesized using the MS method, using glucose as a carbon source and KCl and NaCl as eutectic salts. The synthesis process, material characterization, electrochemical performance, and potential mechanisms underlying the enhanced OER activity of the samples were comprehensively analyzed. The morphological analysis reveals distinct differences between the samples prepared with and without the MS method. The MS method proves beneficial in producing much smaller, thinner, and porous carbon substrates. Further characterizations show that it can help improve the specific surface area, provide active sites at the interface for catalytic reactions, and provide favorable pathways for transferring charges and electrons. The prepared $FeNi_2$/C-MS shows outstanding OER performance in alkaline electrolytes, with an overpotential of 279.4 mV at a current density of 10 mA cm^{-2} and a Tafel slope of 45.7 mV dec^{-1}. The mechanism responsible for the exceptional catalytic performance of $FeNi_2$/C-MS is multifaceted. On the one hand, the change of carbon morphology by the MS method increases the specific surface area and defects, improves the exposure of active sites, accelerates the transfer of charges, and enhances the adhesion and electronic interaction between FeNi and carbon. On the other hand, the molten salt modifies the surface of the metallic particles, increasing the abundance of high-valence Ni and Fe ions and the concentration of M−O and M-OH/OOH bonds. This modification enhances the catalytic activity, making the material more favorable for the oxygen evolution reaction (OER). In conclusion, the FeNi alloy/carbon composite

https://doi.org/10.1021/acsaem.4c02958
ACS Appl. Energy Mater. 2025, 8, 3449−3458

synthesized through the MS method represents a promising catalyst fabrication method. This method paves the way for efficient energy conversion, demonstrating both the potential and significant advantages of the MS method for enhancing electrocatalytic performance in OER applications.

■ ASSOCIATED CONTENT

Supporting Information

The Supporting Information is available free of charge at https://pubs.acs.org/doi/10.1021/acsaem.4c02958.

Photograph of $FeNi_2$/C-MS and $FeNi_2$/C; LSV curves of samples with different reaction temperatures; SEM images of samples with varying temperatures of reaction; XRD pattern of samples with different reaction temperatures; LSV curves of different glucose and metal precursor ratio; SEM-EDS spectrum of FeNi2/C-MS and FeNi2/C; SEM-EDS spectrum of FeNi/C-MS and FeNi/C; SEM-EDS spectrum of Fe_2Ni/C-MS and Fe_2Ni/C-MS; SEM-EDS mapping of $FeNi_2$/C-MS; SEM-EDS mapping of $FeNi_2$/C; SEM image of carbon-MS and carbon; SEM image of FeNi/C-MS and FeNi/C; SEM image of Fe_2Ni/C-MS and Fe_2Ni/C; N_2 adsorption/desorption isotherm and BJH pore-size distribution curves of Fe_2Ni/C-MS; XRD patterns of FeNi/C-MS, FeNi/C, Fe_2Ni/C-MS and Fe_2Ni/C-MS; TEM images of $FeNi_2$/C-MS and $FeNi_2$/C with statistical calculation of diameter; XPS full spectrum of $FeNi_2$/C-MS and $FeNi_2$/C; LSV curves of $FeNi_2$/C-MS, $FeNi_2$/C and bare carbon synthesized by MS; cyclic voltammograms of $FeNi_2$/C-MS and $FeNi_2$/C measured at different scan rates from 20 to 100 mV s^{-1} in 1 M KOH; ECSA normalized polarization curves of $FeNi_2$/C-MS and $FeNi_2$/C; SEM images of $FeNi_2$/C-MS before and after stability test; specific addition amount of different ratios of glucose and metal precursors; SEM-EDS results of Fe_xNi_y/C-MS and Fe_xNi_y/C; BET surface areas and pore size of $FeNi_2$/C-MS and $FeNi_2$/C; atomic ratio of main elements in the $FeNi_2$/C-MS and $FeNi_2$/C based on XPS analysis; area ratio of different valence states of Fe and Ni elements in the $FeNi_2$/C-MS and $FeNi_2$/C based on XPS analysis; ratio of M−O, M-OH and absorbed O in the $FeNi_2$/C-MS and $FeNi_2$/C based on XPS analysis; and comparison of OER performance of different transition metal-based catalysts (PDF)

■ AUTHOR INFORMATION

Corresponding Authors

Takeshi Yanagida − *Institute for Materials Chemistry and Engineering, Kyushu University, Fukuoka 816-8580, Japan; Department of Applied Chemistry, Graduate School of Engineering, The University of Tokyo, Tokyo 113-8656, Japan;* orcid.org/0000-0003-4837-5701; Email: yanagida@g.ecc.u-tokyo.ac.jp

Johnny C. Ho − *Department of Materials Science and Engineering and State Key Laboratory of Terahertz and Millimeter Waves, City University of Hong Kong, Kowloon, Hong Kong SAR 999077, China; Institute for Materials Chemistry and Engineering, Kyushu University, Fukuoka 816-8580, Japan;* orcid.org/0000-0003-3000-8794; Email: johnnyho@cityu.edu.hk

SenPo Yip − *Institute for Materials Chemistry and Engineering, Kyushu University, Fukuoka 816-8580, Japan;* Email: yip.sen.po.472@m.kyushu-u.ac.jp

Authors

Xueda Liu − *Interdisciplinary Graduate School of Engineering Sciences, Kyushu University, Fukuoka 816-8580, Japan;* orcid.org/0009-0000-2314-6780

Dongyuan Song − *Interdisciplinary Graduate School of Engineering Sciences, Kyushu University, Fukuoka 816-8580, Japan;* orcid.org/0009-0008-7753-8593

Quan Quan − *Department of Materials Science and Engineering, City University of Hong Kong, Kowloon, Hong Kong SAR 999077, China*

Dong Chen − *Department of Materials Science and Engineering, City University of Hong Kong, Kowloon, Hong Kong SAR 999077, China*

Hikaru Saito − *Institute for Materials Chemistry and Engineering, Kyushu University, Fukuoka 816-8580, Japan;* orcid.org/0000-0001-9578-1433

Liyuan Dai − *Interdisciplinary Graduate School of Engineering Sciences, Kyushu University, Fukuoka 816-8580, Japan*

Midori Ikeuchi − *Institute for Materials Chemistry and Engineering, Kyushu University, Fukuoka 816-8580, Japan*

Complete contact information is available at: https://pubs.acs.org/10.1021/acsaem.4c02958

Author Contributions

X.L. and S.Y. designed the experiments. X.L. and D.S. synthesized the samples. X.L., D.S., and Q.Q. performed the electrochemical measurements. D.S., D.C., M.I., and H.S. performed the parts of characterizations. X.L. wrote the manuscript. X.L. and D.S. analyzed the data. S.Y., T.Y., and J.C.H. directed this work. All authors discussed and revised the manuscript.

Notes

The authors declare no competing financial interest.

■ ACKNOWLEDGMENTS

This work was funded by "Network Joint Research Center for Materials and Devices" of the Ministry of Education, Culture, Sports, Science and Technology (MEXT) and "Advanced Research Infrastructure for Materials and Nanotechnology in Japan (ARIM)" of the Ministry of Education, Culture, Sports, Science and Technology (MEXT) (Project No. JPMXP1222KU1050).

■ REFERENCES

(1) Chu, S.; Majumdar, A. Opportunities and challenges for a sustainable energy future. *Nature* **2012**, *488* (7411), 294−303.

(2) Chu, S.; Cui, Y.; Liu, N. The path towards sustainable energy. *Nat. Mater.* **2017**, *16* (1), 16−22.

(3) Li, Z.; Jiang, Z.; Zhu, W.; He, C.; Wang, P.; Wang, X.; Li, T.; Tian, L. Facile preparation of CoSe2 nano-vesicle derived from ZIF-67 and their application for efficient water oxidation. *Appl. Surf. Sci.* **2020**, *504*, No. 144368.

(4) Zhao, B.; Zeng, W.; Zhang, W.; Chen, S.; Xu, H.; Liao, Y.; Liao, Y.; Qing, Y.; Wu, Y. Tailored bimetallic synergy of iron−cobalt sulfide anchored to S-doped carbonized wood fiber for high-efficiency oxygen evolution reaction. *Appl. Catal., B* **2024**, *350*, No. 123947.

(5) Tee, S. Y.; Win, K. Y.; Teo, W. S.; Koh, L. D.; Liu, S.; Teng, C. P.; Han, M. Y. Recent progress in energy-driven water splitting. *Adv. Sci.* **2017**, *4* (5), No. 1600337.

(6) Shi, Y.; Zhang, B. Recent advances in transition metal phosphide nanomaterials: synthesis and applications in hydrogen evolution reaction. *Chem. Soc. Rev.* **2016**, *45* (6), 1529−1541.
(7) Zeng, K.; Zhang, D. Recent progress in alkaline water electrolysis for hydrogen production and applications. *Prog. Energy Combust. Sci.* **2010**, *36* (3), 307−326.
(8) Suen, N.-T.; Hung, S.-F.; Quan, Q.; Zhang, N.; Xu, Y.-J.; Chen, H. M. Electrocatalysis for the oxygen evolution reaction: recent development and future perspectives. *Chem. Soc. Rev.* **2017**, *46* (2), 337−365.
(9) Zheng, L.; Luo, H.; Zhong, Y.; Li, W.; Xu, H.; Xiong, F.; Pi, J.; Qing, Y.; Wu, Y. Wood-derived continuously oriented channels coupled with tunable built-in electric fields for efficient oxygen evolution. *Appl. Catal., B* **2025**, *360*, No. 124550.
(10) Qazi, U. Y.; Yuan, C.-Z.; Ullah, N.; Jiang, Y.-F.; Imran, M.; Zeb, A.; Zhao, S.-J.; Javaid, R.; Xu, A.-W. One-step growth of iron−nickel bimetallic nanoparticles on FeNi alloy foils: highly efficient advanced electrodes for the oxygen evolution reaction. *ACS Appl. Mater. Interfaces* **2017**, *9* (34), 28627−28634.
(11) Liu, Y.; Jia, G.; Wu, Q.; Zhang, D.; Wu, J.; Yin, Y.; Sai, S.; Guo, Z.; Cui, X. MOF-derived FeNiCoOX hierarchical hollow nanocages for oxygen evolution reaction. *Mater. Lett.* **2021**, *291*, No. 129564.
(12) Long, X.; Li, J.; Xiao, S.; Yan, K.; Wang, Z.; Chen, H.; Yang, S. A strongly coupled graphene and FeNi double hydroxide hybrid as an excellent electrocatalyst for the oxygen evolution reaction. *Angew. Chem., Int. Ed.* **2014**, *53* (29), 7584−7588.
(13) Zhang, W.; Jia, Q.; Liang, H.; Cui, L.; Wei, D.; Liu, J. Iron doped Ni3S2 nanorods directly grown on FeNi3 foam as an efficient bifunctional catalyst for overall water splitting. *Chem. Eng. J.* **2020**, *396*, No. 125315.
(14) Yan, F.; Wang, Y.; Li, K.; Zhu, C.; Gao, P.; Li, C.; Zhang, X.; Chen, Y. Highly Stable Three-Dimensional Porous Nickel-Iron Nitride Nanosheets for Full Water Splitting at High Current Densities. *Chem. - Eur. J.* **2017**, *23* (42), 10187−10194.
(15) Tian, L.; Wang, K.; Wo, H.; Pang, X.; Zhai, X.; Zhuang, W.; Li, T.; Chen, Y. Bundle-shaped cobalt−nickel selenides as advanced electrocatalysts for water oxidation. *Int. J. Hydrogen Energy* **2019**, *44* (5), 2868−2876.
(16) Zhuang, W.; Li, Z.; Song, M.; Zhu, W.; Tian, L. Synergistic improvement in electron transport and active sites exposure over RGO supported NiP/Fe 4 P for oxygen evolution reaction. *Ionics* **2022**, *28*, 1359−1366.
(17) Wang, J.; Kim, J.; Choi, S.; Wang, H.; Lim, J. A review of carbon-supported nonprecious metals as energy-related electrocatalysts. *Small Methods* **2020**, *4* (10), No. 2000621.
(18) Zhang, K.; Zou, R. Advanced transition metal-based OER electrocatalysts: current status, opportunities, and challenges. *Small* **2021**, *17* (37), No. 2100129.
(19) Wu, Z. P.; Lu, X. F.; Zang, S. Q.; Lou, X. W. Non-noble-metal-based electrocatalysts toward the oxygen evolution reaction. *Adv. Funct. Mater.* **2020**, *30* (15), No. 1910274.
(20) Smith, R. D.; Prévot, M. S.; Fagan, R. D.; Zhang, Z.; Sedach, P. A.; Siu, M. K. J.; Trudel, S.; Berlinguette, C. P. Photochemical route for accessing amorphous metal oxide materials for water oxidation catalysis. *Science* **2013**, *340* (6128), 60−63.
(21) Cui, X.; Ren, P.; Deng, D.; Deng, J.; Bao, X. Single layer graphene encapsulating non-precious metals as high-performance electrocatalysts for water oxidation. *Energy Environ. Sci.* **2016**, *9* (1), 123−129.
(22) Xie, X.; Shang, L.; Shi, R.; Waterhouse, G. I.; Zhao, J.; Zhang, T. Tubular assemblies of N-doped carbon nanotubes loaded with NiFe alloy nanoparticles as efficient bifunctional catalysts for rechargeable zinc-air batteries. *Nanoscale* **2020**, *12* (24), 13129−13136.
(23) Kugabaeva, G. D.; Kydralieva, K. A.; Bondarenko, L. S.; Baimuratova, R. K.; Karpenkov, D. Y.; Golovkova, E. A.; Degtyarenko, P. N.; Golubeva, N. D.; Uflyand, I. E.; Dzhardimalieva, G. I. Polymer-Assisted Synthesis, Structure and Magnetic Properties of Bimetallic FeCo-and FeNi/N-Doped Carbon Nanocomposites. *Magnetochemistry* **2023**, *9* (10), 213.
(24) Xu, Z.; Chen, G.; Yang, F.; Jang, J.; Liu, G.; Xiao, F.; Sun, Y.; Qiu, X.; Chen, W.; Su, D. Graphene-supported Fe/Ni single atoms and FeNi alloy nanoparticles as bifunctional oxygen electrocatalysts for rechargeable zinc-air batteries. *Electrochim. Acta* **2023**, *458*, No. 142549.
(25) He, J.; Hu, B.; Zhao, Y. Superaerophobic electrode with metal@ metal-oxide powder catalyst for oxygen evolution reaction. *Adv. Funct. Mater.* **2016**, *26* (33), 5998−6004.
(26) Liu, Z.; Yu, H.; Dong, B.; Yu, X.; Feng, L. Electrochemical oxygen evolution reaction efficiently boosted by thermal-driving core−shell structure formation in nanostructured FeNi/S, N-doped carbon hybrid catalyst. *Nanoscale* **2018**, *10* (35), 16911−16918.
(27) Deng, S.-Q.; Zhuang, Z.; Zhou, C.-A.; Zheng, H.; Zheng, S.-R.; Yan, W.; Zhang, J. Metal-organic framework derived FeNi alloy nanoparticles embedded in N-doped porous carbon as high-performance bifunctional air-cathode catalysts for rechargeable zinc-air battery. *J. Colloid Interface Sci.* **2023**, *641*, 265−276.
(28) Gu, X.; Liu, Z.; Li, M.; Tian, J.; Feng, L. Surface structure regulation and evaluation of FeNi-based nanoparticles for oxygen evolution reaction. *Appl. Catal., B* **2021**, *297*, No. 120462.
(29) Xiao, M.; Luo, B.; Konarova, M.; Wang, Z.; Wang, L. Molten salt synthesis of atomic heterogeneous catalysts: old chemistry for advanced materials. *Eur. J. Inorg. Chem.* **2020**, *2020* (31), 2942−2949.
(30) Li, J.; Peng, J.; Zeng, K.; Zhong, D.; Xu, K.; Vladimirovich, V. S.; Nzihou, A.; Yang, H.; Chen, H. Solar pyrolysis of algae in molten salt for capacitive carbon preparation. *J. Cleaner Prod.* **2023**, *406*, No. 136898.
(31) McCrory, C. C.; Jung, S.; Peters, J. C.; Jaramillo, T. F. Benchmarking heterogeneous electrocatalysts for the oxygen evolution reaction. *J. Am. Chem. Soc.* **2013**, *135* (45), 16977−16987.
(32) Shu, R.; Li, N.; Li, X.; Sun, J. Preparation of FeNi/C composite derived from metal-organic frameworks as high-efficiency microwave absorbers at ultrathin thickness. *J. Colloid Interface Sci.* **2022**, *606*, 1918−1927.
(33) Setyowati, V. A.; Rois, M. F.; Widiyastuti, W.; Nurkhamidah, S.; Saidatin, N.; Febrianto, M. F. Comparative study of single and bimetal-nitrogen-doped carbon prepared by polymerization and direct pyrolysis. *Results Eng.* **2022**, *13*, No. 100332.
(34) Broström, M.; Enestam, S.; Backman, R.; Mäkelä, K. Condensation in the KCl−NaCl system. *Fuel Process. Technol.* **2013**, *105*, 142−148.
(35) Sakita, A.; Vallés, E.; Della Noce, R.; Benedetti, A. Novel NiFe/NiFe-LDH composites as competitive catalysts for clean energy purposes. *Appl. Surf. Sci.* **2018**, *447*, 107−116.
(36) Díez, N.; Fuertes, A. B.; Sevilla, M. Molten salt strategies towards carbon materials for energy storage and conversion. *Energy Storage Mater.* **2021**, *38*, 50−69.
(37) Gupta, S. K.; Mao, Y. A review on molten salt synthesis of metal oxide nanomaterials: Status, opportunity, and challenge. *Prog. Mater. Sci.* **2021**, *117*, No. 100734.
(38) Feng, Y.; Zhang, H.; Fang, L.; Mu, Y.; Wang, Y. Uniquely monodispersing NiFe alloyed nanoparticles in three-dimensional strongly linked sandwiched graphitized carbon sheets for high-efficiency oxygen evolution reaction. *ACS Catal.* **2016**, *6* (7), 4477−4485.
(39) Liu, X.; Giordano, C.; Antonietti, M. A facile molten-salt route to graphene synthesis. *Small* **2014**, *10* (1), 193−200.
(40) Qi, L.; Tang, X.; Wang, Z.; Peng, X. Pore characterization of different types of coal from coal and gas outburst disaster sites using low temperature nitrogen adsorption approach. *Int. J. Min. Sci. Technol.* **2017**, *27* (2), 371−377.
(41) Liu, H.; Zhu, S.; Zhang, Y.; Song, H.; Zhang, Y.; Chang, Y.; Hou, W.; Han, G. Unveiling Superior Capacitive Behaviors of One-Pot Molten Salt-Engineered B, N Co-Doped Porous Carbon Sheets. *Small* **2023**, *19* (40), No. 2204119.

https://doi.org/10.1021/acsaem.4c02958
ACS Appl. Energy Mater. 2025, 8, 3449−3458

(42) Yang, Y.; Ma, Y.; Lu, C.; Li, S.; Zhu, M. Molten salt technique for the synthesis of carbon-based materials for supercapacitors. *Green Chem.* **2023**, *25* (24), 10209−10234.
(43) Ban, F.; Majid, S. R.; Huang, N. M.; Lim, H. Graphene oxide and its electrochemical performance. *Int. J. Electrochem. Sci.* **2012**, *7* (5), 4345−4351.
(44) Sure, J.; Shankar, A. R.; Ramya, S.; Mudali, U. K. Molten salt corrosion of high density graphite and partially stabilized zirconia coated high density graphite in molten LiCl−KCl salt. *Ceram. Int.* **2012**, *38* (4), 2803−2812.
(45) Zhang, X.; Chen, Y.; Wang, B.; Chen, M.; Yu, B.; Wang, X.; Zhang, W.; Yang, D. FeNi nanoparticles embedded porous nitrogen-doped nanocarbon as efficient electrocatalyst for oxygen evolution reaction. *Electrochim. Acta* **2019**, *321*, No. 134720.
(46) Liu, J.; Dong, S.; He, Q.; Yang, S.; Xie, M.; Deng, P.; Xia, Y.; Li, G. Facile preparation of Fe3O4/C nanocomposite and its application for cost-effective and sensitive detection of tryptophan. *Biomolecules* **2019**, *9* (6), 245.
(47) Liu, Z.; Yu, X.; Yu, H.; Xue, H.; Feng, L. Nanostructured FeNi3 incorporated with carbon doped with multiple nonmetal elements for the oxygen evolution reaction. *ChemSusChem* **2018**, *11* (16), 2703−2709.
(48) Ma, Y.; Dai, X.; Liu, M.; Yong, J.; Qiao, H.; Jin, A.; Li, Z.; Huang, X.; Wang, H.; Zhang, X. Strongly coupled FeNi alloys/NiFe2O4@ carbonitride layers-assembled microboxes for enhanced oxygen evolution reaction. *ACS Appl. Mater. Interfaces* **2016**, *8* (50), 34396−34404.
(49) Yolshina, L.; Yolshina, V.; Pershina, S.; Pryakhina, V. Study of thermal stability of hierarchical structured carbon composite flakes. *Diamond Relat. Mater.* **2021**, *119*, No. 108556.
(50) Gao, Y.; Hu, S.; Zhou, Y.; Zhang, S. Template-free synthesis of biomass-derived hierarchically mesoporous carbon with ultra-small FeNi nanoparticles for oxygen evolution reaction. *Int. J. Hydrogen Energy* **2019**, *44* (51), 27806−27815.
(51) Li, Z.; Qiu, G.; Shen, Y.; Wang, X.; Zhuang, W.; Li, J.; Song, M.; Wang, P.; Tian, L. Ultrafine trimetallic oxyphosphide nanoparticles for efficient electrochemical overall water splitting. *J. Alloys Compd.* **2020**, *820*, No. 153161.
(52) Sun, C.; Zhang, H.; Liu, H.; Zheng, X.; Zou, W.; Dong, L.; Qi, L. Enhanced activity of visible-light photocatalytic H2 evolution of sulfur-doped g-C3N4 photocatalyst via nanoparticle metal Ni as cocatalyst. *Appl. Catal., B* **2018**, *235*, 66−74.
(53) Feng, Y.; Liu, S.; Shen, Y.; Akhtar, K.; Bakhsh, E. M.; Khan, S. B.; Wang, M. Outstanding oxygen evolution reaction properties released at the interface of NiMoO4 and FeNi layer double hydroxide heterostructures. *Electrochim. Acta* **2024**, *474*, No. 143511.
(54) Xiao, H.; Shin, H.; Goddard, W. A., III Synergy between Fe and Ni in the optimal performance of (Ni, Fe) OOH catalysts for the oxygen evolution reaction. *Proc. Natl. Acad. Sci. U. S. A.* **2018**, *115* (23), 5872−5877.
(55) Trotochaud, L.; Young, S. L.; Ranney, J. K.; Boettcher, S. W. Nickel−iron oxyhydroxide oxygen-evolution electrocatalysts: the role of intentional and incidental iron incorporation. *J. Am. Chem. Soc.* **2014**, *136* (18), 6744−6753.
(56) Bates, M. K.; Jia, Q.; Doan, H.; Liang, W.; Mukerjee, S. Charge-transfer effects in Ni−Fe and Ni−Fe−Co mixed-metal oxides for the alkaline oxygen evolution reaction. *ACS Catal.* **2016**, *6* (1), 155−161.
(57) Wei, L.; Du, M.; Zhao, R.; Zhang, Y.; Zhang, L.; Li, L.; Yang, S.; Su, J. Active sites engineering on FeNi alloy/Cr3C2 heterostructure for superior oxygen evolution activity. *J. Colloid Interface Sci.* **2024**, *653*, 1075−1084.
(58) Liu, Z.; Ma, Y.; Gu, W.; Yuan, C.; Teng, F. Facile synthesis of MoxC-FeNi@ NC with an OER activity superior to RuO2 and IrO2/C. *J. Phys. Chem. Solids* **2020**, *147*, No. 109578.
(59) Ding, D.; Huang, J.; Tang, J.; Zhang, S.; Deng, X. Preparation of FeNi-based nanoporous amorphous alloy films and their electrocatalytic oxygen evolution properties. *Int. J. Hydrogen Energy* **2023**, *48* (52), 19984−19994.

https://doi.org/10.1021/acsaem.4c02958
ACS Appl. Energy Mater. 2025, 8, 3449−3458